

## Absolute Measurement of Laser Ionization Yield in Atmospheric Pressure Range Gases over 14 Decades

D. Woodbury<sup>1</sup>, R. M. Schwartz,<sup>1</sup> E. Rockafellow<sup>1</sup>, J. K. Wahlstrand,<sup>2</sup> and H. M. Milchberg<sup>1,\*</sup>

<sup>1</sup>*Institute for Research in Electronics and Applied Physics, University of Maryland, College Park, Maryland 20742, USA*

<sup>2</sup>*Physical Measurement Laboratory, National Institute of Standards and Technology, Gaithersburg, Maryland 20899, USA*



(Received 5 November 2019; published 6 January 2020)

Strong-field ionization is central to intense laser-matter interactions. However, standard ionization measurements have been limited to extremely low density gas samples, ignoring potential high density effects. Here, we measure strong-field ionization in atmospheric pressure range air, N<sub>2</sub>, and Ar over 14 decades of absolute yield, using mid-IR picosecond avalanche multiplication of single electrons. Our results are consistent with theoretical rates for isolated atoms and molecules and quantify the ubiquitous presence of ultralow concentration gas contaminants that can significantly affect laser-gas interactions.

DOI: [10.1103/PhysRevLett.124.013201](https://doi.org/10.1103/PhysRevLett.124.013201)

The unification of tunneling ionization and multiphoton ionization (MPI) of atoms in intense laser fields by Keldysh in 1965 [1] provided an analytic foundation for strong-field laser physics [2–6], but measurements of the transition from MPI to tunneling had to await later advances in short pulse lasers [7–10]. This transition is characterized in atomic units by the dimensionless Keldysh parameter  $\gamma = (2\chi_p)^{1/2}\omega/E_0$ , where  $\chi_p$  is the atom's ionization potential,  $E_0$  is the peak laser field, and  $\omega$  is the laser frequency. At moderate intensity  $I$  ( $\gamma \gg 1$ , MPI regime), the ionization yield  $Y$  is proportional to  $E_0^{2n} (\propto I^n)$ , while at higher intensities or longer wavelengths ( $\gamma < 1$ ), the transition to tunneling and barrier suppression ionization [7,9] is characterized by  $Y \propto I^{p < n}$ , where  $n$  is the integer number of photons needed to exceed  $\chi_p$ . These early measurements were conducted in extremely low density gases (typically  $\sim 10^8$ – $10^{12}$  cm<sup>-3</sup>) in order to prevent ionization products interacting with background gas or experiencing space charge effects in transit to high voltage detectors [7,9,11]. However, many applications of strong-field ionization, such as high harmonic generation [12] or high intensity pulse propagation [13], occur at atomic densities many orders of magnitude higher, where density-dependent ionization may be important.

Recent theoretical work, for example, suggests many-body effects in high density gases leads to an additional ionization channel which is important at lower laser intensities: excitation-induced dephasing (EID) [14–17]. If “standard” isolated atom multiphoton or tunneling ionization is viewed as the result of optical-field-induced dephasing of bound state-continuum coherence, which spoils the adiabatic following of the electron population in the strong, highly detuned optical field, then at elevated densities it was proposed that additional dephasing from Coulomb interaction with electrons in nearby atoms enhances ionization beyond the isolated atom process.

EID calculations [14] predict that the additional yield scales nearly linearly with density and is proportional to  $I^2$  (in strong contrast with  $I^n$  scaling for MPI), and is nearly independent of target species and laser wavelength. Of particular interest to our experiments, EID predicts yields  $Y$  in the range  $10^{-9}$ – $10^{-7}$  for 1 TW/cm<sup>2</sup>,  $\lambda = 1$ – $10$   $\mu$ m, 100 fs pulses in a variety of atmospheric pressure range gases [14–17], with  $Y \propto I^2$  until a transition to the isolated atom rate at higher intensities. For example, for a  $\lambda = 1$   $\mu$ m, 100 fs pulse in hydrogen, Ref. [16] showed  $Y \propto I^2$  up to  $Y \sim 10^{-6}$  at  $I \sim 20$  TW/cm<sup>2</sup>, transitioning to MPI yields ( $\propto I^{10}$ ) of  $\sim 10^{-5}$  at  $I \sim 40$  TW/cm<sup>2</sup>. While prior ionization yield measurements at atmospheric pressure [18,19] have shown reasonable agreement with isolated atom rates, they were limited to  $Y > \sim 10^{-5}$  for a  $\lambda = 800$  nm driver, precluding investigation of EID ionization.

The potential effect of EID ionization is significant, especially when its boost to plasma density would have a commensurately larger effect on the refractive index experienced by longer wavelength lasers. For example, under conditions where standard ionization is negligible, EID was invoked to explain a recent experiment observing self-channeling of a  $\lambda = 10.2$   $\mu$ m,  $\sim 1$  TW/cm<sup>2</sup> peak intensity CO<sub>2</sub> laser pulse over 20 Rayleigh ranges in air [20], a process requiring plasma generation to offset Kerr self-focusing.

In this Letter, we use avalanche ionization driven by a picosecond, mid-IR *probe* laser pulse to measure absolute ionization yields over 14 decades ( $10^{-16}$ – $10^{-2}$ ) from femtosecond near-IR and mid-IR *pump* pulse irradiation of atmospheric pressure range air, nitrogen, and argon (0.5–3 bar). This represents an unprecedented dynamic range with a single setup, with a sensitivity achievable by no other method we are aware of. In avalanche ionization, free electrons (here initially generated by femtosecond pump pulses) gain sufficient energy through probe-driven

collisions until they ionize neutral atoms or molecules, leading to an exponential growth factor  $e^{\nu_i t}$  in the local number of electrons, where  $\nu_i$  is the effective collisional ionization rate. Growth saturates due to depletion of neutral molecules (for example, at 5% full single ionization of air, electron density  $\sim 10^{18} \text{ cm}^{-3}$  and  $\nu_i$  is reduced by 5%).

Figure 1 shows the experimental setup. The femtosecond pump pulse, synchronized to the avalanche-driving probe, was either in the near-IR ( $\lambda = 1024 \text{ nm}$ ,  $274 \pm 10 \text{ fs}$ ) or in the mid-IR ( $\lambda = 3.9 \mu\text{m}$ ,  $85 \pm 5 \text{ fs}$ ) and focused to peak intensities of 1–100  $\text{TW}/\text{cm}^2$ , with intensity control provided by a wave plate and polarizer. Avalanche ionization was driven by a positively chirped  $\sim 10 \text{ mJ}$ ,  $50 \text{ ps}$ ,  $\lambda = 3.9 \mu\text{m}$  probe pulse focused to intensities  $\sim 1\text{--}1.5 \text{ TW}/\text{cm}^2$  at a  $1/e^2$  intensity radius (waist) of  $w_0 = 70 \mu\text{m}$ . The peak probe intensity defines a breakdown volume inside of which the intensity exceeds a threshold value leading to detectable avalanches (see Supplemental Material [21]). Crucially, the mid-IR avalanche driver eliminates driver-supplied MPI electrons from the seed population [25,26]. All three pulses were derived from a 20 Hz chirped pulse amplification (OPCPA) system [27], with details of focal spot measurements, breakdown volume, and absolute intensity uncertainty ( $\sim \pm 10\%$ ) given in the Supplemental Material [21].

For low yields up to  $\sim 10^{-11}$ , visible avalanche breakdowns are local to individual seed electrons, with radial migration of avalanche-liberated electrons limited to  $< \sim 10 \mu\text{m}$  by electron and ambipolar diffusion during the 50 ps probe pulse [26,28]. Thus, breakdowns are isolated and were counted by imaging, with a 16-bit

low-noise CMOS camera, the overlap of the pump pulse and probe breakdown volume [Fig. 1(a)] inside a sealed gas cell filled with air, nitrogen, or argon passed through a  $0.01 \mu\text{m}$  rating particulate filter. In this regime, the occurrence of breakdowns is statistical, requiring multishot averaging. In order to determine peak yield  $Y_0$  corresponding to the peak intensity  $I_0$ , we use  $N = \int_V Y_0 [I(r, z)/I_0]^m dV$ , where  $N$  is the average number of counts measured,  $I(r, z)$  is the spatially varying pump intensity with peak value  $I_0$  over the probe breakdown volume  $V$ , and the yield is observed to scale as  $I^m$ . A counterpropagating ( $\theta = 0^\circ$ ) pump-probe geometry maximized the overlap volume and, hence, sensitivity. As higher pump intensity increased the number of seed electrons beyond  $\sim 10$ , individual breakdowns upstream interfered with probe driving of downstream avalanches. Switching to a perpendicular geometry ( $\theta = 90^\circ$ ) reduced the overlap volume  $\sim 100\times$ , eliminating this propagation effect at higher yield. While the small volume for  $\theta = 90^\circ$  prevents reliably imaging more than 1 breakdown per shot, counting the incidence of no breakdowns allowed us to infer the Poisson mean up to  $\sim 4$  breakdowns/shot, since a Poisson distribution with mean value  $\mu$  has a probability  $P(0) = 1 - e^{-\mu}$  of observing no counts. With the pump blocked, breakdowns occurred in  $\sim 1$  out of 100–1000 shots due to probe-induced MPI of a contaminant (see below).

As the yield (and seed electron density) increases even further,  $\lesssim 10^{-10}\text{--}10^{-2}$ , adjacent incipient avalanche sites become closer than the electron diffusion length and it is no longer possible to resolve and count breakdowns. However, the avalanche is now seeded by a well-defined local

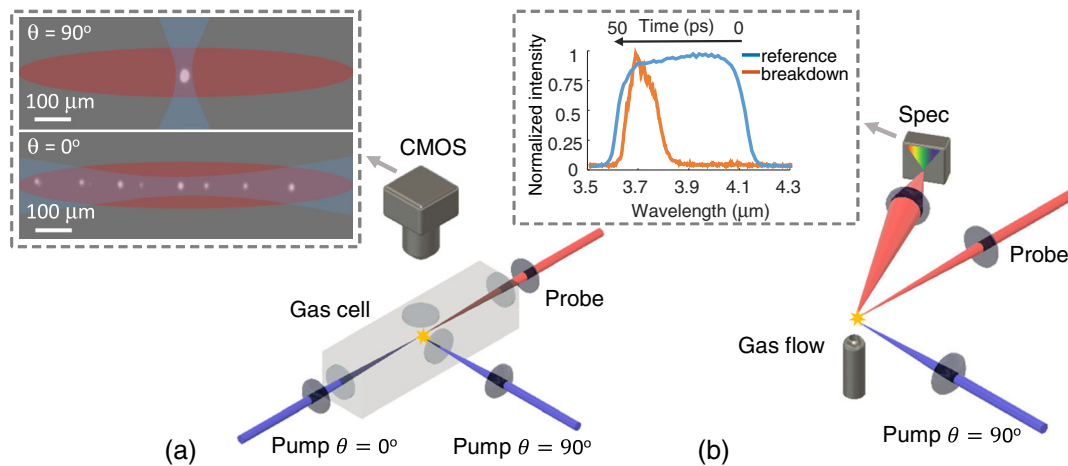


FIG. 1. Experimental setup. (a) Breakdown counting ( $I < 10 \text{ TW}/\text{cm}^2$ ). A positively chirped,  $\lambda = 3.6\text{--}4.2 \mu\text{m}$ , 50 ps mid-IR laser probe pulse was focused into a gas cell to drive avalanche breakdowns seeded by electrons liberated by either a counterpropagating ( $\theta = 0^\circ$ ) or a perpendicularly directed ( $\theta = 90^\circ$ ) pump pulse (274 fs,  $\lambda = 1024 \text{ nm}$  or 85 fs,  $\lambda = 3.9 \mu\text{m}$ ). The inset shows, for each geometry, sample images of individually seeded breakdowns, collected by camera CMOS, and overlaid with pump pulse focal volume (blue) and the probe pulse breakdown threshold volume (red). (b) Breakdown time advance ( $I > 10 \text{ TW}/\text{cm}^2$ ). Pump-induced initial plasma density and corresponding yield are determined from breakdown timing encoded in the backscatter spectrum of the chirped mid-IR probe pulse. Backscatter is collected by spectrometer (Spec), with example incident and backscattered spectra and corresponding timing shown. Here, breakdowns are observed directly above a  $\sim 5 \text{ mm}$  gas flow orifice.

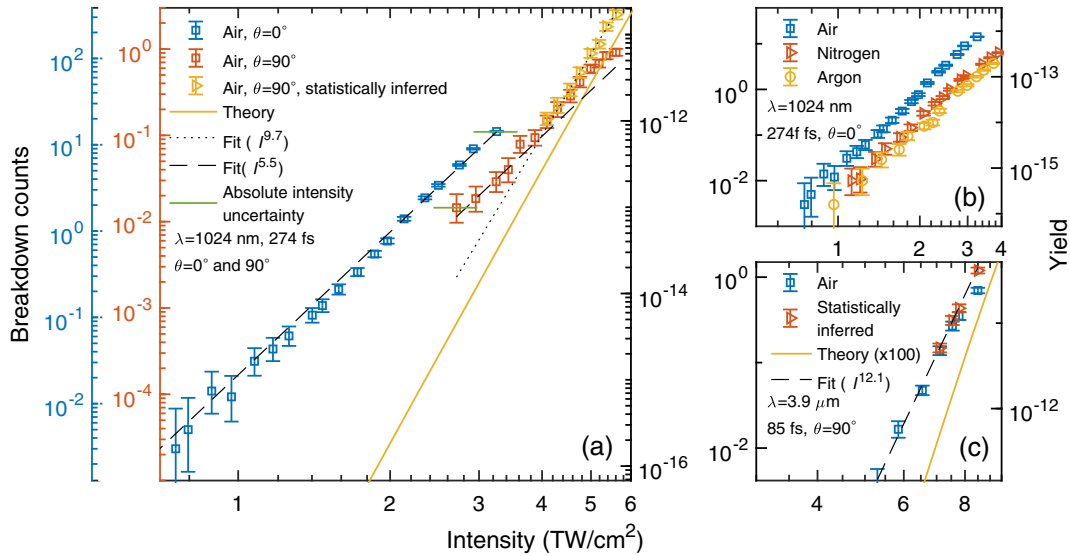


FIG. 2. Ionization yield measured in breakdown counting regime ( $I < 10$  TW/cm<sup>2</sup>). (a) Breakdown counts and corresponding yields  $Y_{1024\text{ nm}}$  in  $\theta = 0^\circ$  and  $\theta = 90^\circ$  geometry. For  $I > \sim 4$  TW/cm<sup>2</sup>,  $Y_{1024\text{ nm}} \propto I^{9.7}$ , consistent with MPI of oxygen ( $\chi_p \sim 12.1$  eV) and for  $I < \sim 4$  TW/cm<sup>2</sup>,  $Y_{1024\text{ nm}} \propto I^{5.5}$ , consistent with MPI of a contaminant with  $\chi_p \sim 6$  eV. Error bars correspond to a Poissonian 95% confidence interval [31]. Horizontal bars on the  $0^\circ$  and  $90^\circ$  plots reflect absolute intensity uncertainty when switching between geometries. The overlaid theory curve plots the yield based on standard N<sub>2</sub> and O<sub>2</sub> molecular ionization rates [6,10]. (b) Comparison of  $Y_{1024\text{ nm}}$  for atmospheric pressure air, N<sub>2</sub>, and Ar for  $I < \sim 4$  TW/cm<sup>2</sup> ( $\theta = 0^\circ$ ), showing  $Y_{1024\text{ nm}} \propto I^{5.5}$  for all three gases. (c)  $Y_{3.9\text{ }\mu\text{m}}$  for atmospheric pressure air ( $\theta = 90^\circ$ ). The overlaid ionization theory curve for 80/20 N<sub>2</sub>/O<sub>2</sub> is multiplied by 100. In panels (a) and (c), saturated counts were inferred statistically from the incidence of no breakdowns occurring, as described in the text.

electron density such that one can measure a deterministic avalanche time,  $\tau = \ln(N_{ef}/N_{e0})/\nu_i$ , where  $N_{e0}$  is the seed electron density,  $\nu_i$  is the electron density collisional growth rate, and  $N_{ef}$  is a final (detectable) electron density [29,30]. By employing our previously demonstrated chirped probe-backscatter breakdown timing method [26], we measure the breakdown time advance  $\Delta t_{adv} = \tau_{driver} - \tau$ , where  $\tau_{driver} = 50$  ps is the avalanche driver duration and  $\Delta t_{adv}$  corresponds to the reddest (earliest) wavelength of the chirped probe pulse detectable in the backscattered spectrum at a detection threshold  $N_{ef} \sim 10^{18}$  cm<sup>-3</sup>. The spectrum is collected by a single shot mid-IR spectrometer [26], with setup and example spectra shown in Fig. 1(b). Wavelength-to-time correspondence of the chirped driver was established using a cross-correlation with the  $\lambda = 1024$  nm beam.

Figures 2–4 together show femtosecond pulse ionization yields  $Y$  spanning 14 orders of magnitude. For lower peak intensities of 0.6–10 TW/cm<sup>2</sup>, where yields are determined from counting individual breakdowns, Fig. 2 plots  $Y_{1024\text{ nm}}$  for air [Fig. 2(a)], a comparison of  $Y_{1024\text{ nm}}$  for air, N<sub>2</sub>, and Ar [Fig. 2(b)], and  $Y_{3.9\text{ }\mu\text{m}}$  for air [Fig. 2(c)], all at atmospheric pressure. Here,  $\gamma_{1024\text{ nm}} > 3$  and  $\gamma_{3.9\text{ }\mu\text{m}} < 0.9$ , in the MPI and tunneling regime, respectively. The corresponding average breakdown counts per shot are shown on separate scales. In Fig. 2(a), the curves for  $\theta = 0^\circ$  and  $\theta = 90^\circ$  are horizontally offset owing to peak intensity uncertainty of  $\sim \pm 10\%$  (horizontal bars) in each geometry [21].

Theoretical isolated molecule yields were calculated using a rate valid for arbitrary  $\gamma$  by properly treating the Coulomb correction in the multiphoton limit  $\gamma \gg 1$  [2,6]. This “standard” yield for air (80/20 N<sub>2</sub>/O<sub>2</sub>), using effective potentials for N<sub>2</sub> and O<sub>2</sub> [10], is plotted as the yellow curves in Figs. 2(a) and 2(c), with the curve in Fig. 2(c) scaled up by 100 $\times$ .

Best fits to the data points for all three gases give  $Y_{1024\text{ nm}} \propto I^{5.5 \pm 0.3}$  (for  $I < \sim 4$  TW/cm<sup>2</sup>) and  $Y_{3.9\text{ }\mu\text{m}} \propto I^{12.1 \pm 0.8}$ , with measured yields orders of magnitude greater than standard theory. For air at  $I > \sim 4$  TW/cm<sup>2</sup>, the yield dependence transitions to  $Y_{1024\text{ nm}} \propto I^{9.7 \pm 1.0}$ , consistent with the expected MPI scaling of  $I^{10}$  for oxygen, the most readily ionized air constituent ( $\chi_p \sim 12.1$  eV). The  $\sim 2\times$  offset between experiment and theory in this range is consistent with  $\sim 10\%$  experimental uncertainty in absolute intensity [21] and the lack of species-specific atomic structure in the theoretical rate [6]. The range of exponents is determined by the 95% confidence interval for linear fitting to data on a log-log scale. We note that in this plot, the background level of counts from the mid-IR probe pulse alone is  $\sim 10^{-3}$  for the low intensity pump points (for  $\theta = 0^\circ$ ) and  $\sim 10^{-2}$  for  $\theta = 90^\circ$ , as discussed in Ref. [21].

These results strongly suggest that the ionization yield at lower intensity originates from a contaminant common to all three gases, whose purity is discussed in Ref. [21]. Further supporting the presence of a contaminant, when the cell was filled with bottled, high purity air passed through a

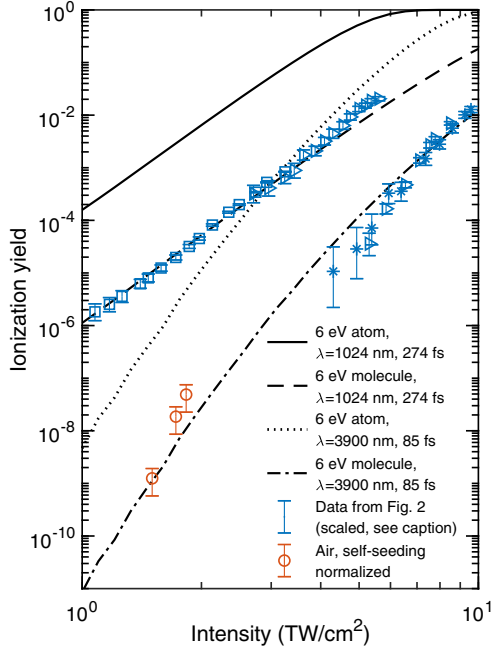


FIG. 3. Comparison of contaminant yield with isolated atom or molecule theory. Counts in air ( $\theta = 0^\circ$ , squares;  $\theta = 90^\circ$ , triangles) and argon ( $\theta = 90^\circ$ , stars) are shifted to overlap with theoretical curves for comparison. The red points (open circles) are from 50 ps probe self-seeded avalanches, normalized to the other  $\lambda = 3.9 \mu\text{m}$  data on the plot (see Fig. S2 and discussion in Ref. [21]). Two theory curves were generated for each wavelength: a 6 eV atom and a 6 eV molecule. The molecule calculation employs a shape factor (0.5) to account for changes to its tunneling potential [10]. The calculated contaminant yields, together with the absolute yields determined in Fig. 2, suggest a contaminant concentration in the range  $10^{-11}$ – $10^{-9}$ , assuming a shape factor bounded between 1 (atom) and 0.5 (typical molecule).

Supelcarb part-per-billion level hydrocarbon trap, the ionization yield dropped by a factor of  $\sim 4$ , with the intensity scaling remaining the same [21]. The gas cell experiment was repeated for air pressures of 0.5–3 bar. At all pressures, the yield scaling at lower intensity followed  $Y_{1024 \text{ nm}} \propto I^{5.5 \pm 0.3}$ , consistent with the presence of the contaminant. At higher intensity, the yield dependence transitioned to the MPI scaling of oxygen, as in Fig. 2(a).

As shown in Fig. 3, fitting the yield scaling to the standard isolated atom or molecule ionization rate [6] suggests the contaminant species has an ionization potential  $\chi_p \sim 6$  eV and an approximate concentration of  $\sim 10^{-11}$ – $10^{-9}$ . The  $\lesssim 2 \text{ TW}/\text{cm}^2$  (red) points with  $Y_{3.9 \mu\text{m}} \propto I^{19 \pm 8}$  were obtained from counting breakdowns self-seeded by the  $\lambda = 3.9 \mu\text{m}$  probe and were normalized to short pulse results as described in Ref. [21], and are also consistent with MPI of a  $\chi_p \sim 6$  eV contaminant. We note that early MPI experiments indicated the presence of low ionization potential contaminants in all laboratory gases; these were considered to be the source for seed electrons in air avalanche breakdown experiments [7,11]. However, the

concentration and yield of these seed sources could not be quantified as in the present work.

Figure 4 covers the transition from MPI of air and  $\text{N}_2$  to tunneling ionization, with  $3 > \gamma_{1024 \text{ nm}} > 0.75$ . In this regime, we used our breakdown time advance diagnostic. Conversion from  $\Delta t_{\text{adv}}$  to yield was calibrated by data from the direct imaging measurements at  $\sim 6 \text{ TW}/\text{cm}^2$  [Fig. 3(a)] and previous absolute measurements of yield at  $\sim 100 \text{ TW}/\text{cm}^2$  [18], with direct interpolation between the points assuming a constant growth rate for a flattop probe pulse intensity, as explained in greater detail in Ref. [21]. Measured yields and theory show agreement within a factor of 10 over the full intensity range despite the simplistic assumption of constant growth rate. Accounting for the probe pulse temporal envelope and chirp-dependent heating would bring the curves into even closer agreement [21]. We note that the growth rate,  $\nu_i = 0.55 \text{ ps}^{-1}$ , extracted from this interpolation also applies to laser-air interactions with a different wavelength but the same numerical value of  $I\lambda^2$ , and can be used to benchmark simulations of high intensity, picosecond laser-driven avalanche.

Our femtosecond pump ionization yield measurements can be summarized as follows. At lower intensities (Figs. 2 and 3,  $< \sim 4 \text{ TW}/\text{cm}^2$ ), where the biggest relative contributions from EID ionization are expected, pump wavelength-dependent scaling of yield is consistent with ionization of a low-level contaminant with  $\chi_p \sim 6$  eV.

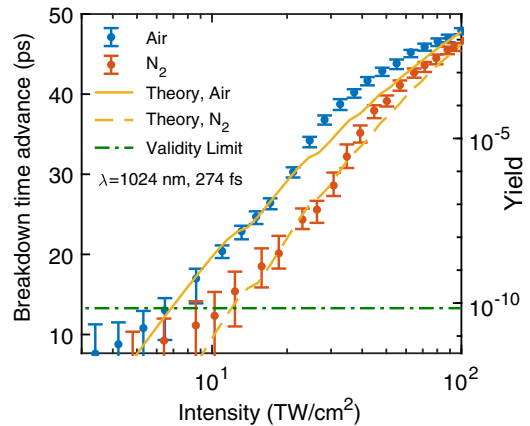


FIG. 4. Ionization yield measured in breakdown time advance regime ( $I > 10 \text{ TW}/\text{cm}^2$ ). Ionization yields in air and  $\text{N}_2$  determined by breakdown time advance  $\Delta t_{\text{adv}}$ , with theoretical yields overlaid. The horizontal dot-dashed line indicates the limit above which  $\Delta t_{\text{adv}}$  is deterministically correlated with seed electron density. Below this level, individual breakdowns do not overlap during their initial growth phase, and breakdown timing is determined by statistical placement of seed electrons in the pump volume (see Fig. S4 in Ref. [21]). Conversion to yield was benchmarked with imaging results from Fig. 2(a) and previous measurements [18]. The points at each intensity give the mean  $\Delta t_{\text{adv}}$ , and error bars show the standard deviation of timing measurements due to either statistical placement of seeds (low intensity) or  $\sim 5\%$  fluctuations in probe pulse energy (higher intensity).

Neither the wavelength-independent  $I^2$  scaling nor the wavelength-insensitive absolute yield suggested by EID is observed, and the yields are a factor of  $10^6$  lower than those predicted [15–17]. The source of disagreement is unclear, calling for a reexamination of the theoretical work. In the higher intensity range  $4 < I < 10$  TW/cm<sup>2</sup> of Fig. 2, the yield at  $\lambda = 1024$  nm transitions into MPI of O<sub>2</sub>, while it is in the tunneling regime of the contaminant for  $\lambda = 3.9$   $\mu$ m. In Fig. 4, at higher intensities up to 100 TW/cm<sup>2</sup> and the transition from MPI to tunneling, the ionization yield is in good agreement with isolated atom or molecule theory.

We note that avalanches seeded by low ionization potential contaminants could have a significant effect on long wavelength infrared filamentation and be consistent with the observations of self-channeling of  $\lambda = 10.6$   $\mu$ m, terawatt-level CO<sub>2</sub> laser pulses [20] without the need for EID ionization. Not only can a long-wave IR pulse easily ionize the  $\chi_p \sim 6$  eV contaminant, but the  $\lambda^2$  dependence of collisional heating and free-electron polarizability [17,20,32] renders such a pulse quite sensitive to the free electrons and the subsequent avalanche it self-generates.

In conclusion, we have shown that avalanche breakdown using picosecond mid-IR probe pulses is a sensitive diagnostic of extremely low electron densities—achieving an unprecedented dynamic range of 14 orders of magnitude, with picosecond and few micron resolution. We measure ionization generated by femtosecond pump pulses in several gases in the atmospheric pressure range and find that the yield at lower laser intensities  $\sim 1$  TW/cm<sup>2</sup> is consistent with MPI of a ubiquitous parts-per-trillion contaminant, and is not dependent on predicted many-body effects, while yield at higher intensities ( $> \sim 10$  TW/cm<sup>2</sup>) is consistent with MPI or tunneling ionization of isolated molecules. In particular, our avalanche method enables measurement of intermediate electron densities in a range ( $10^8$ – $10^{13}$  cm<sup>-3</sup>) inaccessible with other standard techniques without sacrificing spatial or temporal resolution [33–37].

The authors thank J. Isaacs and P. Sprangle for useful discussions and for assistance in simulating avalanche breakdowns. This work is supported by the Air Force Office of Scientific Research (AFOSR) (FA9550-16-1-0121, FA9550-16-1-0259), Office of Naval Research (ONR) (N00014-17-1-2705), Defense Threat Reduction Agency (DTRA) (HDTRA11510002), and the National Science Foundation (NSF) (PHY1619582). D. W. acknowledges support from the DOE NNSA SSGF program under DE-NA0003864.

\*Corresponding author.  
milch@umd.edu

[1] L. V. Keldysh, *Sov. Phys. JETP* **20**, 1307 (1965).  
[2] A. M. Perelomov, V. S. Popov, and M. V. Terent'ev, *Sov. Phys. JETP* **23**, 924 (1966).

[3] A. M. Perelomov and V. S. Popov, *Sov. Phys. JETP* **25**, 336 (1967).  
[4] M. V. Ammosov, N. B. Delone, and V. P. Krainov, *Sov. Phys. JETP* **64**, 1191 (1986).  
[5] V. S. Popov, *Phys. Usp.* **47**, 855 (2004).  
[6] S. V. Popruzhenko, V. D. Mur, V. S. Popov, and D. Bauer, *Phys. Rev. Lett.* **101**, 193003 (2008).  
[7] S. L. Chin, F. Yergeau, and P. Lavigne, *J. Phys. B* **18**, L213 (1985).  
[8] D. Strickland and G. Mourou, *Opt. Commun.* **55**, 447 (1985).  
[9] S. Augst, D. D. Meyerhofer, D. Strickland, and S. L. Chin, *J. Opt. Soc. Am. B* **8**, 858 (1991).  
[10] A. Talebpour, J. Jang, and S. L. Chin, *Opt. Commun.* **163**, 29 (1999).  
[11] S. L. Chin, *Can. J. Phys.* **48**, 1314 (1970).  
[12] T. Popmintchev *et al.*, *Science* **336**, 1287 (2012).  
[13] A. Couairon and A. Mysyrowicz, *Phys. Rep.* **441**, 47 (2007).  
[14] K. Schuh, J. Hader, J. V. Moloney, and S. W. Koch, *Phys. Rev. E* **89**, 033103 (2014).  
[15] K. Schuh, J. Hader, J. V. Moloney, and S. W. Koch, *J. Opt. Soc. Am. B* **32**, 1442 (2015).  
[16] K. Schuh, J. V. Moloney, and S. W. Koch, *Phys. Rev. E* **93**, 013208 (2016).  
[17] K. Schuh, M. Kolesik, E. M. Wright, J. V. Moloney, and S. W. Koch, *Phys. Rev. Lett.* **118**, 063901 (2017).  
[18] J. K. Wahlstrand, S. Zahedpour, A. Bahl, M. Kolesik, and H. M. Milchberg, *Phys. Rev. Lett.* **120**, 183901 (2018).  
[19] A. Sharma, M. N. Slipchenko, M. N. Shneider, X. Wang, K. A. Rahman, and A. Shashurin, *Sci. Rep.* **8**, 2874 (2018).  
[20] S. Tochitsky *et al.*, *Nat. Photonics* **13**, 41 (2019).  
[21] See Supplemental Material at <http://link.aps.org/supplemental/10.1103/PhysRevLett.124.013201> for laser pulse characterization, breakdown threshold, probe self-seeding of avalanche, and calibration of yield to time advance, which includes Refs. [22–24].  
[22] C. G. Morgan, *Rep. Prog. Phys.* **38**, 621 (1975).  
[23] A. W. Ali, NRL Memorandum Report No. 5187, 1983, <https://apps.dtic.mil/docs/citations/ADA145158>.  
[24] A. W. Ali, NRL Memorandum Report No. 5400, 1984, <https://apps.dtic.mil/docs/citations/ADA133211>.  
[25] R. M. Schwartz, D. Woodbury, J. Isaacs, P. Sprangle, and H. M. Milchberg, *Sci. Adv.* **5**, eaav6804 (2019).  
[26] D. Woodbury, R. M. Schwartz, and H. M. Milchberg, *Optica* **6**, 811 (2019).  
[27] G. Andriukaitis, T. Balčiūnas, S. Ališauskas, A. Pugžlys, A. Baltuška, T. Popmintchev, M.-C. Chen, M. M. Murnane, and H. C. Kapteyn, *Opt. Lett.* **36**, 2755 (2011).  
[28] F. F. Chen, *Introduction to Plasma Physics and Controlled Fusion* (Plenum Press, New York, 1974).  
[29] J. Isaacs, C. Miao, and P. Sprangle, *Phys. Plasmas* **23**, 033507 (2016).  
[30] J. Isaacs, D. Woodbury, and P. Sprangle, *Proc. SPIE Int. Soc. Opt. Eng.*, 11010E (2019).  
[31] F. Garwood, *Biometrika* **28**, 437 (1936).  
[32] P. Panagiotopoulos, M. Kolesik, S. W. Koch, E. M. Wright, S. Tochitsky, and J. V. Moloney, *J. Opt. Soc. Am. B* **36**, G33 (2019).  
[33] M. N. Shneider and R. B. Miles, *J. Appl. Phys.* **98**, 033301 (2005).

- [34] Y.-H. Chen, S. Varma, T. M. Antonsen, and H. M. Milchberg, *Phys. Rev. Lett.* **105**, 215005 (2010).
- [35] D. Abdollahpour, S. Suntsov, D. G. Papazoglou, and S. Tzortzakis, *Opt. Express* **19**, 16866 (2011).
- [36] V. P. Drachev, Y. I. Krasnikov, and P. A. Bagryansky, *Rev. Sci. Instrum.* **64**, 1010 (1993).
- [37] C. O. Laux, T. G. Spence, C. H. Kruger, and R. N. Zare, *Plasma Sources Sci. Technol.* **12**, 125 (2003).